THE M_W 7.6 DUSKY SOUND EARTHQUAKE OF 2009: PRELIMINARY REPORT

Bill Fry[1], Stephen Bannister[1], John Beavan[1], Lara Bland[1], Brendon Bradley[1, 2], Simon Cox[1], Jim Cousins[1], Nora Gale[1], Graham Hancox[1], Caroline Holden[1], Richard Jongens[1], William Power[1], Gegar Prasetya[1], Martin Reyners[1], John Ristau[1], Russell Robinson[1], Sergey Samsonov[1, 3], Kate Wilson[1] and the GeoNet team.

SUMMARY

The M_w 7.6 Dusky Sound earthquake of July 15th, 2009, was the largest magnitude earthquake in New Zealand since the devastating 1931 Hawke's Bay event (Ms 7.8). The earthquake was sufficiently large to generate at least a 2.3 m wave at Passage Point. Despite its large magnitude, this event resulted in relatively minimal damage when compared to worldwide events of a similar size. This can be explained as a fortunate combination of the sparse population of the area and the specific physical characteristics of the earthquake. Centroid Moment Tensor (CMT) solutions define the rupture surface as a low-angle plane and finite fault inversions confirm the slip occurred on the interface between the eastward-subducting Australian plate and overriding Pacific plate, initiating at about 30 km depth and rupturing upward and southwestward to about 15 km depth. The oceanward rupture directivity likely contributed to the lower intensity of measured ground motion than might be expected for such a large, shallow event. The amount of radiated seismic energy from the earthquake was relatively small, and far fewer landslides were triggered from this event than from the 2003 M_w 7.2 Fiordland event.

TECTONIC SETTING AND RECENT SEISMICITY

In the Fiordland region, the motion of the Australian plate relative to the Pacific plate is c. 34 mm/yr at 062º (DeMets *et al.*, 1994; Figure. 1). Thus the plate boundary is characterised by highly oblique convergence. The convergent component of the relative plate motion is being accommodated largely by southeasterly subduction of the Australian plate, while the along-strike component of motion is mostly accommodated by the Alpine fault. The detailed morphology of the dipping seismic zone associated with the subducted Australian plate has been revealed by earthquakes relocated by Eberhart-Phillips & Reyners (2001). The dipping seismic zone steepens from south to north, becoming near-vertical below about 75 km depth north of Doubtful Sound. This steepening is accompanied by a sharp change in strike of the subduction zone. South of Doubtful Sound, the average strike is 023º, whereas north of Doubtful Sound it is 040º.

The focal mechanisms and depths of large historical earthquakes in Fiordland have been determined by Doser *et al.* (1999). In the period 1918-62, none of these large events appears to have occurred at the shallow part of the plate interface. Rather, they appear to have been associated with complex deformation within both the subducted and overlying plates. However, in the last 30 years there has been a series of large earthquakes in the Fiordland region, many of which have been interpreted as shallow interplate thrust events (Figure 1). These events surround the Dusky Sound earthquake rupture zone, suggesting that this latest event has filled a gap in interplate slip along the subduction zone.

GEONET MONITORING

Rapid Response

The initial GeoNet analysis placed the earthquake's hypocentre in Dusky Sound underneath Resolution Island in Fiordland with a local magnitude of 6.6. About an hour after the main shock, the USGS released a new moment magnitude for the earthquake placing it at 7.8. This was a revision from their original estimation of 8.0. The USGS value was based on teleseismic data, and as such, was not affected by saturation effects which yield spuriously low magnitudes when solving for higher-frequency data measured close to the epicentre. The GeoNet website provided the public with information about the earthquake, peaking at two million hits per hour within the first hour of the event.

The Dusky Sound main shock was very well recorded on the GeoNet seismograph and GPS networks. Of the 47 National Network stations, which each contain a continuously recording broadband seismometer and a strong motion accelerometer, 45 of the broadband seismometers and 18 of the accelerometers recorded the event. Eighty one of the 94 continuously recording short-period seismic stations and 60 of the 232 triggered strong motion accelerometers also recorded

[1] *GNS Science, Lower Hutt*

[2] *Chuo University, Tokyo, Japan*

[3] *University of Western Ontario, London Ontario, Canada*

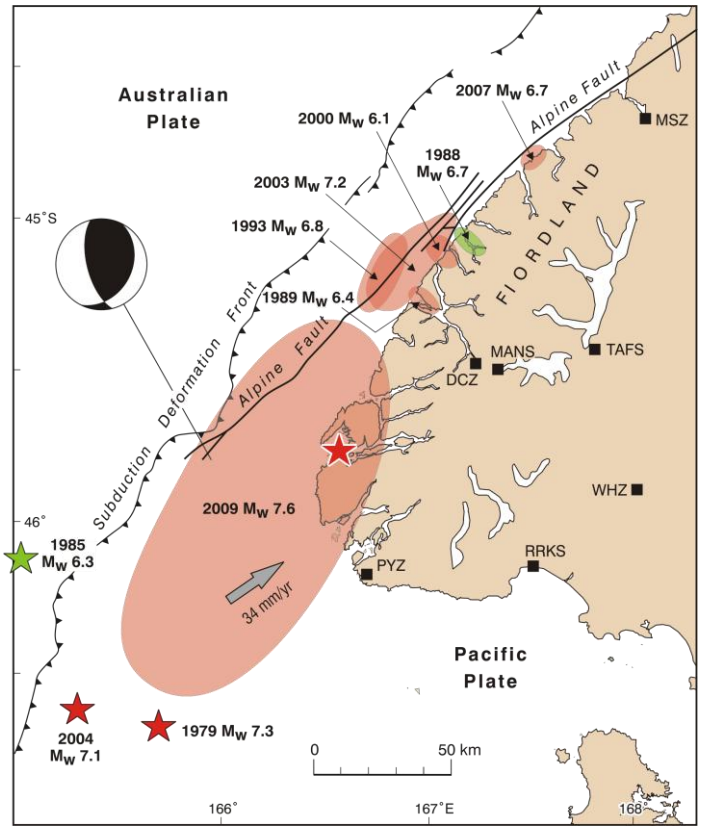

Figure 1: ***Tectonic setting of the Dusky Sound earthquake. The epicentre of the earthquake is shown by the large red star, and the rupture zone is approximated by the distribution of the first five days of aftershocks (large pink region). The beachball shows the USGS centroid moment tensor solution for the mainshock, and the arrow indicates the velocity of the Australian plate relative to the Pacific plate (DeMets et al., 1994). Filled squares indicate GeoNet seismographs and strong motion recorders which recorded the earthquake. Large earthquakes in the last 30 years surrounding the Dusky Sound event are also shown either by their aftershock zones, or by stars marking their epicentres in the offshore southwestern region where aftershock distributions are poorly determined. Pink denotes events interpreted as interplate, and green denotes intraslab events.***

the event. Eight of the 137 continuous GPS sites had permanent co-seismic displacements of greater than 5 mm.

GeoNet seismic monitoring in the Fiordland region consists of two National Network seismic stations, Puysegur Point (PYZ) and Deep Cove (DCZ). In order to more precisely locate aftershocks, GeoNet deployed six portable short period instruments close to the epicentre (Figure 2). The coastal sites, Dagg Sound, Breaksea Sound, Duck Cove, and Lake Frazer, were positioned along a coastal transect proximal to the offshore Puysegur subduction zone with spacing of ~20 km. The inland stations, Supper Cove and Last Cove, form an inland transect between PYZ and DCZ that provides a two-dimensional geometry to the array with spacing of ~30 km. The precise locations of the aftershocks will be used to infer local fault structure and provide insight into the nature of the Fiordland subduction zone.

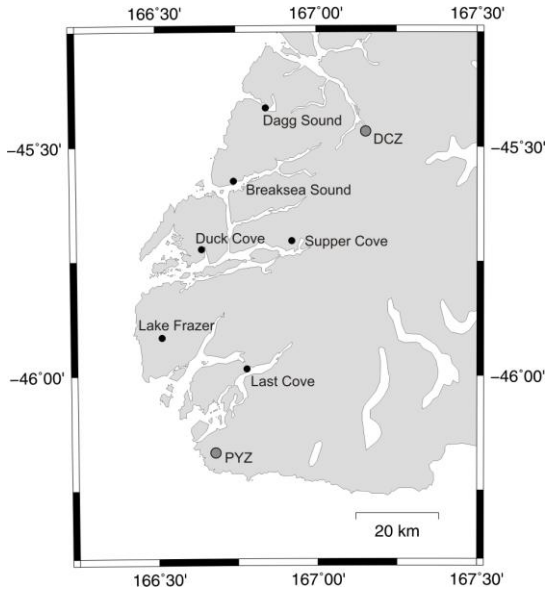

Figure 2: ***Six portable short period seismic stations (black circles) were deployed in the south western Fiordland region to complement the existing GeoNet national network stations (grey circles), which each contain a broadband seismometer and a strong motion accelerometer.***

Felt reports and damage

The earthquake was felt widely across New Zealand, and generated considerable interest from scientists, the media, and the public. The GeoNet Website (www.geonet.org.nz) was an important tool in the distribution and collection of information about the earthquake. On July 15th the website was visited by over 47,000 individual users, ten times the daily average for the week preceding the quake. Within 12 hours of the main shock almost 1900 people had registered 'felt reports'. In total, over 3000 felt reports were submitted, from as far away as Orewa, north of Auckland. However, a M5.5 earthquake occurred near Taranaki in the North Island about 15 minutes after the main Dusky Sound shock. Consequently, some of the North Island felt reports cannot be unambiguously assigned to the Dusky Sound event. The information given in each of the reports submitted was used to assign a Modified Mercalli

(MM) value to the intensity of the shaking experienced. The intensities ranged from MM3 in the upper North Island (Auckland, Bay of Plenty and Hawke's Bay) to MM7 in Invercargill, where a number of houses were damaged.

THE MAINSHOCK RUPTURE DETERMINED FROM SEISMOLOGICAL STUDIES

To solve for a detailed slip-time distribution of earthquake rupture, we inverted data from 4 strong motion sites of the GeoNet network (Figure 3). Seismograms were band-pass filtered between 0.01 and 0.1 Hz and integrated to yield velocity data. We modelled one fault plane of 27 degree strike, 33 degree dip as defined by our preferred moment tensor solution. This fault plane attitude corresponds closely with the strike (27º) of the southern Fiordland subduction zone and the average dip of the plate interface across the rupture (31 º). The fault plane area is 140 by 80 km². It is divided into 700 4x4 km^2 subfaults. We solved for two elliptical rupture areas distributed randomly within the fault plane with variable rupture velocity, slip and rake (Francois-Holden *et al.*, 2007). Our best-fitting slip distribution derived from the strong motion observations (Figure 3) is characterized by a large rupture area of about 36 by 44 km, with a maximum slip of 8.9 m at 23 km depth on the main fault plane occurring 16 seconds after the rupture began. The rupture starts downdip at about 38 km depth and propagates upward reaching a depth of 8 km. The rupture velocity obtained from the inversion is 2.62 km/s. The inverted slip direction (or rake angle) is 154 degrees. The moment value calculated for our preferred solution is 2.72×10^{20} Nm.

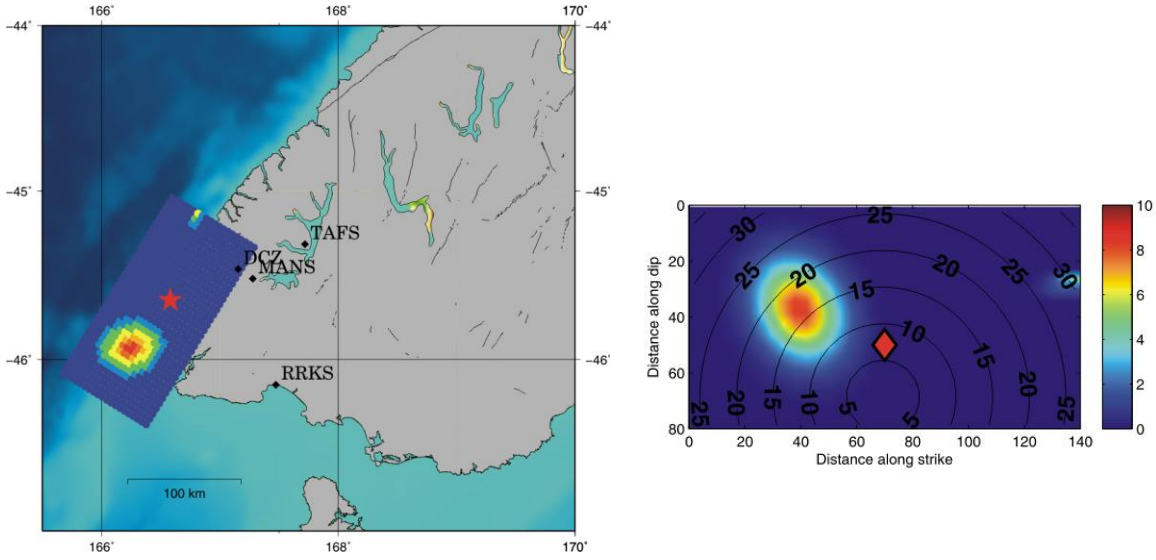

Figure 3: ***Left, the rectangle is the surface projection of the modelled fault plane. Black diamonds show strong motion stations used in the inversion for source modelling. Right, final slip and rupture time distribution on a 140 by 80 km fault plane. The slip distribution is characterized by patch of high slip occurring south and updip of the hypocentre with a reverse type mechanism.***

Finite fault inversions for the mainshock rupture using teleseismic data are in general agreement and are reasonably compatible with our solution based on strong motion data (e.g. http://earthquake.usgs.gov/eqcenter/eqinthenews/2009/us2009jcap/#scitech , http://www.eri.u-tokyo.ac.jp/topics/200907_NewZealand/index_e.html). These inversions, as well as our inversion of geodetic data (discussed later) confirm that the low angle nodal plane of the centroid moment tensor solution (see Figure 1) corresponds to the fault plane. We can thus be confident that the earthquake involved thrusting on the shallow part of the plate interface.

STRESS ANALYSIS

Previous workers have proposed that a power-law acceleration of seismic moment release (AMR) precedes large earthquakes (Bowman and King, 2001; Bowman *et al.*, 1998, Jaume and Sykes, 1999). Under this theory, seismicity and stress distributions behave in a predictable way throughout the seismic cycle surrounding big earthquakes (Robinson *et al.*, 2005). In retrospect, it is clear that the 2009 earthquake marked the culmination of at least a 40 year power-law distribution of accelerating moment release in the wider Fiordland region (Figure 4). Also, the thrusting that occurred during the Resolution Ridge earthquake of 1985 (see Figure 1 for location) may also be precursory, insofar as such compressional outer-rise events tend to occur seaward of seismic gaps in seismically coupled subduction zones, or equivalently just prior to large subduction thrust earthquakes (Christensen & Ruff, 1983).

One stable feature of the rupture was the relatively small amount of radiated seismic energy – the corresponding energy magnitude (M_e) determined by the USGS was only 7.3. This indicates an apparent stress of only 0.2 MPa, on the low side of the average for subduction thrust events (0.3 MPa; Choy *et al.*, 2006). By way of contrast, the 2003 M_w 7.2 Fiordland interplate earthquake, which caused significantly more landslides than the Dusky Sound earthquake, had an apparent stress of 0.5 MPa. However, the redistribution of stresses following this event likely increased the stress on the offshore portion of the Alpine Fault at depth. Starting with the rupture

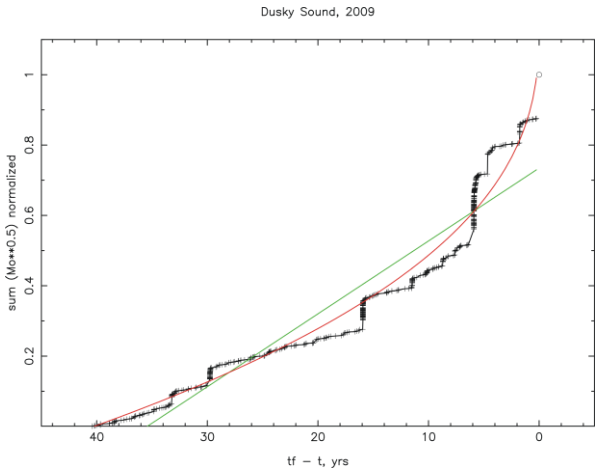

Figure 4: ***Black crosses show accumulated moment release (AMR) over the last 40 years of epicentres within a radius of 344 km of the Dusky Sound epicentre. AMR following the Dusky Sound earthquake is plotted as a circle. The green line is the best linear fit. The red curve is the best exponential fit. The moment of the main shock was not used in the fitting. Over the past 40 years, AMR in Fiordland is well fit with a power-law distribution.***

model generated from inversions of geodetic data, we calculate static strain resulting from the earthquake. This strain is then transformed to a regional stress field using Hooke's Law. The resulting stress tensor is subsequently rotated to define the induced Coulomb failure stress (δCFS) on our planar geometric model of the southernmost Alpine Fault (Figure 5). These calculations show a positive δCFS of about 2 bars on deeper areas of the fault, while shallower regions experienced a negative δCFS, or stress drop. This calculation is in good agreement with results obtained from geodetic studies discussed later in this paper. The effect of the stress loading on the lower portions of the fault is difficult to interpret (e.g., Stein, 1999; King and Cocco, 2001). One large and outstanding question relating to the increased likelihood of a major Alpine Fault rupture resulting from the loading is the present stress state of the Alpine Fault at depth.

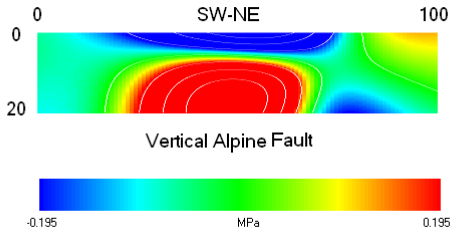

Figure 5: ***Calculated change in Coulomb Failure Stress (dCFS) on the southernmost Alpine Fault as a result of the redistribution of stresses released during the Dusky Sound earthquake. Red areas experienced an increase of stress of approximately 2 bars. Areas in blue experienced a negative dCFS, or stress drop.***

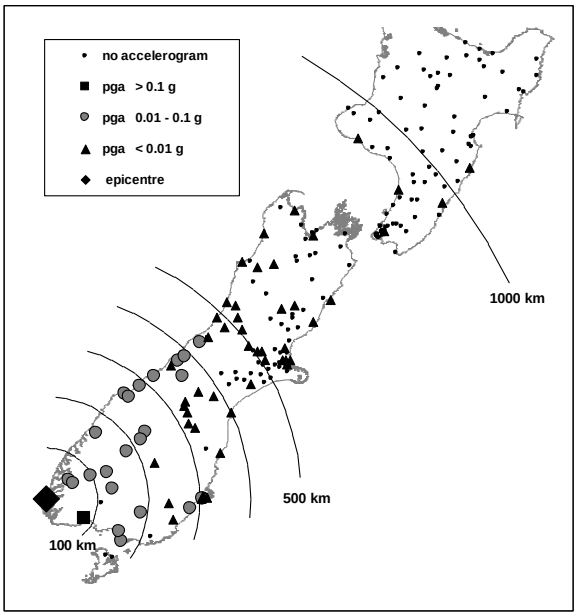

Figure 6: ***Locations of strong-motion sensors at the time of the Dusky Sound Earthquake of 15th July 2009, with peak ground acceleration levels indicated where strong-motion (acceleration) recordings were obtained. More acceleration data are potentially available because 35 of the "no-accelerogram" sites are National Network seismograph sites that are likely to have provided velocity records from the earthquake.***

STRONG GROUND MOTION SERIES

Seventy-four strong ground motion sensors were triggered and recorded the event (Figure 6). The strongest peak ground acceleration (PGA) of 0.14g was from Rarakau located 17 km west of Tuatapere and a little over 80 km from the fault rupture surface (Table 1). The measured PGA from the accelerograms closest to the source (Deep Cove and Manapouri at source distances of 40 and 45 km respectively)

Table 1: Strong-motion data recorded within 400 km source distance of the Dusky Sound Earthquake of 15th July 2009. The ground subsoil categories are as defined in NZS1170.5 (Standards New Zealand, 2004).

Source Distance (km)	Peak Ground Acceleration (g)			Site Code	Name of Recording Site	Ground Subsoil Category
	Vertical	Horiz. 1	Horiz. 2			
40	0.049	0.068	0.067	DCZ	Deep Cove	A
45	0.024	0.044	0.033	MANS	Manapouri	A
82	0.060	0.110	0.148	RRKS	Rarakau	C
65	0.034	0.078	0.091	TAFS	Te Anau Fire Station	D
96	0.013	0.023	0.019	MLZ	Mavora Lakes	B
106	0.027	0.041	0.031	MOSS	Mossburn School	D
151	0.012	0.024	0.026	ICCS	Invercargill City Council	C
110	0.016	0.023	0.029	MSZ	Milford Sound	A
162	0.013	0.023	0.026	NZAS	New Zealand Aluminium Smelter	D
138	0.035	0.032	0.048	QTPS	Queenstown Police Station	D
173	0.017	0.034	0.024	GORS	Gore District Council	D
170	0.011	0.010	0.015	WKZ	Wanaka	B
182	0.006	0.008	0.009	EAZ	Earnscleugh	B
185	0.021	0.029	0.038	WNPS	Wanaka National Park Headquarters	D
216	0.004	0.004	0.004	TUZ	Tuapeka	B
233	0.003	0.005	0.000	BDCS	Balclutha District Council	B
202	0.004	0.008	0.009	JCZ	Jackson Bay	A
202	0.019	0.070	0.049	NSBS	Neils Beach	D
261	0.004	0.009	0.010	TMBS	Taieri Mouth Beach School	C
231	0.013	0.028	0.031	HDWS	Haast DOC Workshop	D
277	0.005	0.007	0.006	DUNS	Dunedin Delta Substation	B
278	0.003	0.004	0.006	DCDS	Dunedin Civil Defence	C
278	0.006	0.015	0.018	DKHS	Dunedin Kings High School	D?
279	0.010	0.024	0.021	SKFS	St Kilda Fire Station	D
279	0.003	0.004	0.005	DGNS	Dunedin GNS	C
286	0.002	0.002	0.003	OPZ	Otago Peninsula	B
266	0.003	0.005	0.004	BENS	Benmore	B
266	0.009	0.013	0.022	LPLS	Lake Paringa Lodge	D
275	0.002	0.003	0.003	AVIS	Aviemore	B
273	0.003	0.005	0.003	LBZ	Lake Benmore	B
274	0.003	0.008	0.006	TWAS	Twizel Area School	D
280	0.004	0.007	0.004	PKIS	Pukaki	B
312	0.004	0.005	0.005	OAMS	Oamaru North Otago Museum	C
302	0.005	0.005	0.005	FOZ	Fox Glacier	B
305	0.004	0.008	0.010	MCNS	Mount Cook Annex	C - D
312	0.002	0.005	0.004	TKAS	Tekapo A	B
319	0.006	0.010	0.011	FGPS	Fox Glacier DOC	D
333	0.004	0.008	0.006	FDCS	Fairlie District Council	D
335	0.007	0.011	0.009	FJDS	Franz Josef DOC	D
350	0.003	0.005	0.007	TRCS	Timaru Roncalli College	C
375	0.006	0.011	0.011	HAFS	Harihari Fire Station	D
391	0.003	0.007	0.006	WVAS	Waitaha Valley	D

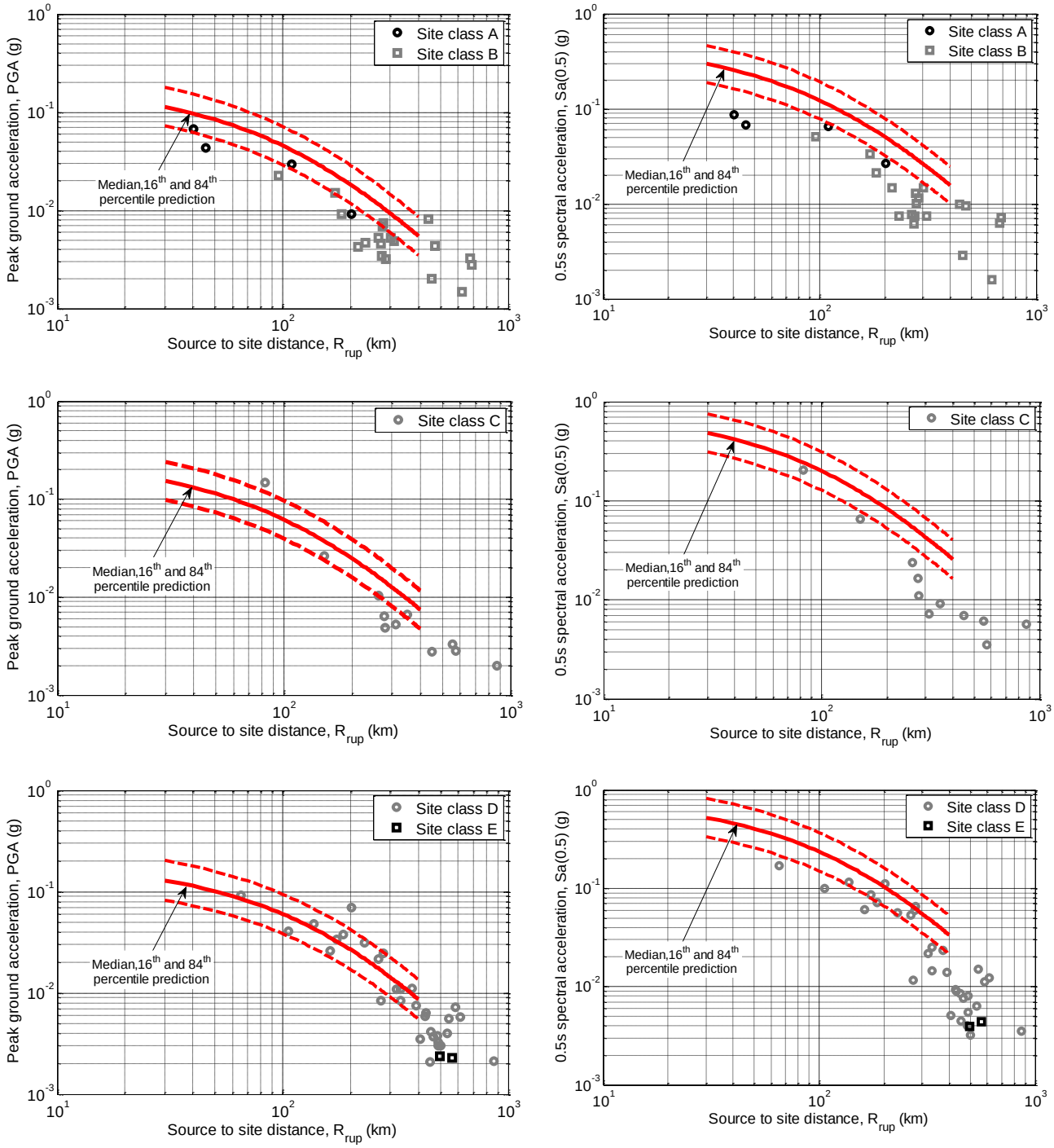

Figure 7: ***Attenuation of peak ground acceleration and 0.5 second response spectral ordinates with source-to-site distance. The prediction was only developed for source-to-site distances up to 400 km.***

were 0.07 and 0.04g. Attenuation of PGA and 0.5 second spectral acceleration (Sa (0.5)) with source-to-site distance observed in strong ground motion recordings were predicted using the McVerry *et al* (2006) prediction equation (Figure 7). Both PGA and Sa (0.5) tend to be over-predicted by the model for site classes A and B (hard rock and rock). For site classes C and D, which are predominately those sites whose previous recordings were used to develop the model, the model prediction is notably more accurate.

Due to the remoteness of the earthquake, there was a paucity of proximal strong ground motion measurements. Only five stations were located within 100 km of the earthquake rupture. This lack of strong motion recordings close to the rupture is the primary reason for the absence of intense ground motion recordings from this earthquake and sensitivity of the model to PGA values near the epicenter. Our strong ground motion model overpredicts the observed horizontal response spectra at periods longer than 0.3 seconds for the four ground motions recorded closest to the fault rupture (Figure 8). There is an improved comparison at periods shorter than 0.15 seconds (Figure 8b and 8c), and there seems to be evidence of rich frequency content affecting the 0.7-0.9s spectral ordinates. The Rarakau ground motion is very similar to the predicted median ground motion at periods beyond 0.3 seconds, and above the predicted values for shorter periods (Figure 8c). At Te Anau (a site class D site), the ground motions contain considerable site-specific effects, with the predominant period of the response spectra around 3 seconds. Such site-specific effects, presumably resulting from the near-surface geologic

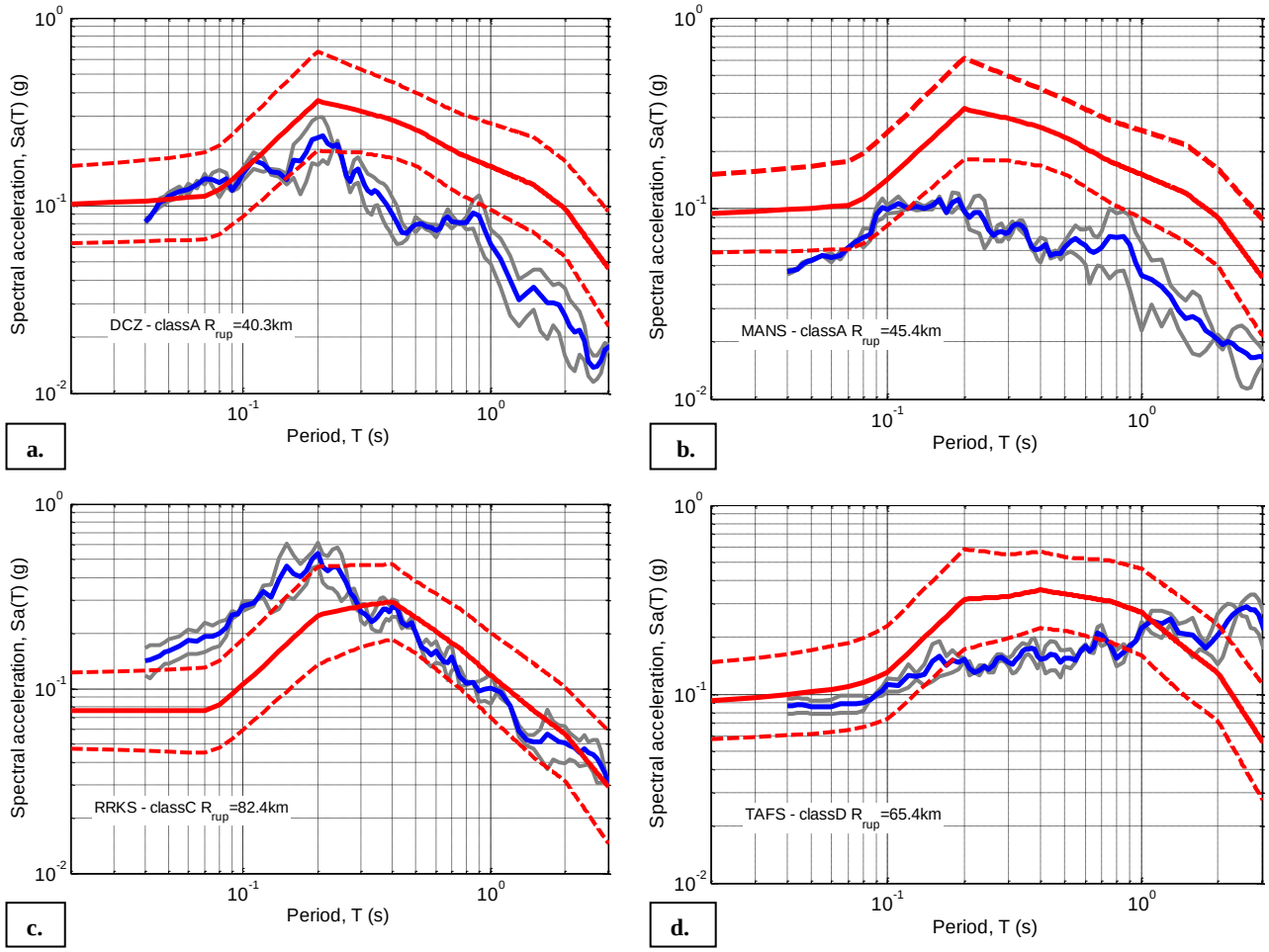

Figure 8: ***Comparison of response spectral spectra of the four ground motions recorded within 100 km of the earthquake rupture extent: (a) Deep Cove (DCZ); (b) Manapouri (MANS); (c) Rarakau (RRKS); and (d) Te Anau (TAFS). Model predictions are shown in red; spectrum of individual horizontal components in grey; and their geometric mean in blue.***

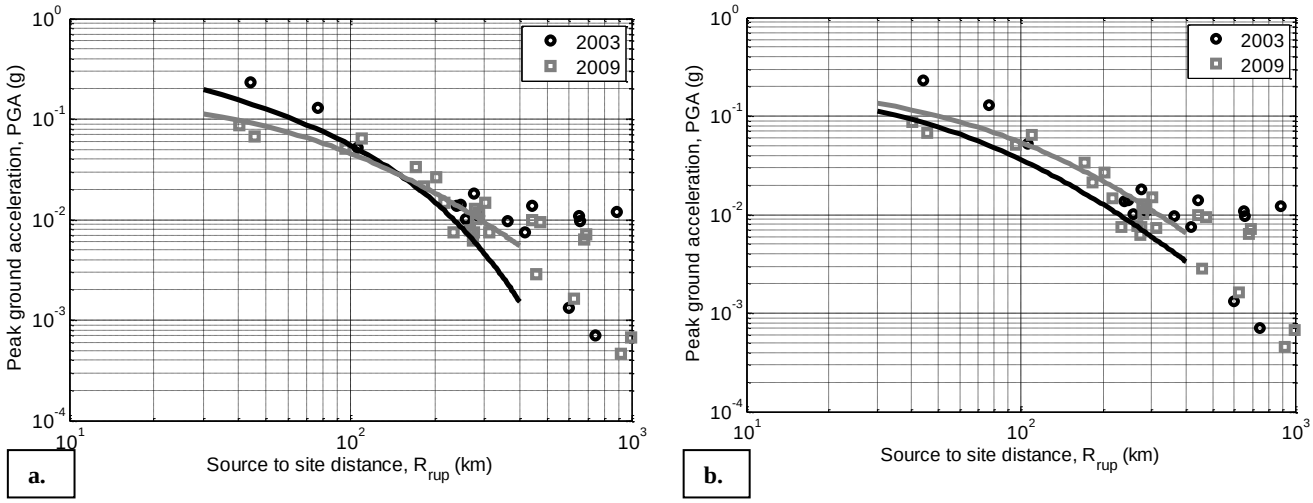

Figure 9: ***Comparison of the attenuation of peak ground acceleration (PGA) with source-to-site distance (R_{rup}) for the 2003 and 2009 Fiordland earthquakes: (a) 2003 event assumed to have a reverse crustal focal mechanism; and (b) 2003 event assumed to have a subduction interface focal mechanism.***

structure of the site, cannot be accurately predicted by the current model.

The measured PGA resulting from the 2009 and 2003 Fiordland earthquakes are very similar (Figure 9). Some uncertainty exists as to the mechanism of the 2003 event. The median ground motion predictions of the two likely options (reverse crustal and subduction interface) are shown in Figures 9a and 9b, respectively. The predicted median ground motions from the models clearly indicate the sensitivity of the modeling of ground motions to source mechanism.

SOURCE CHARACTERIZATION

Moment tensor solutions

High quality seismic broadband data recorded by the GeoNet network were used to calculate regional moment tensor (RMT) solutions for a large number of aftershocks. A brief description of the moment tensor method is given here; Ristau (2008) provides a detailed overview of the RMT method in New Zealand. In 2003 the GeoNet project began a major upgrade to the New Zealand seismograph network, and currently there are more than 40 three-component broadband seismometers in New Zealand which provide high quality seismic data suitable for RMT analysis. It is now possible to routinely calculate moment tensor solutions for New Zealand earthquakes with Mw ≥~ 3.5 – 4.0. RMT solutions at GeoNet are calculated using code developed by Doug Dreger at the University of California, Berkeley Seismological Laboratory (Dreger and Helmberger, 1993; Pasyanos *et al.*, 1996; Dreger, 2003). RMT analysis differs from teleseismic moment tensor analysis (e.g. Global CMT Project or USGS moment tensor solutions) in two important ways. First, only regional waveform data (source-receiver distances of 1000 km or less) are used, and second, we employ region-specific velocity models. For M ≤ 5.0, there is little very low-frequency energy in the waveforms and the velocity model used to calculate the

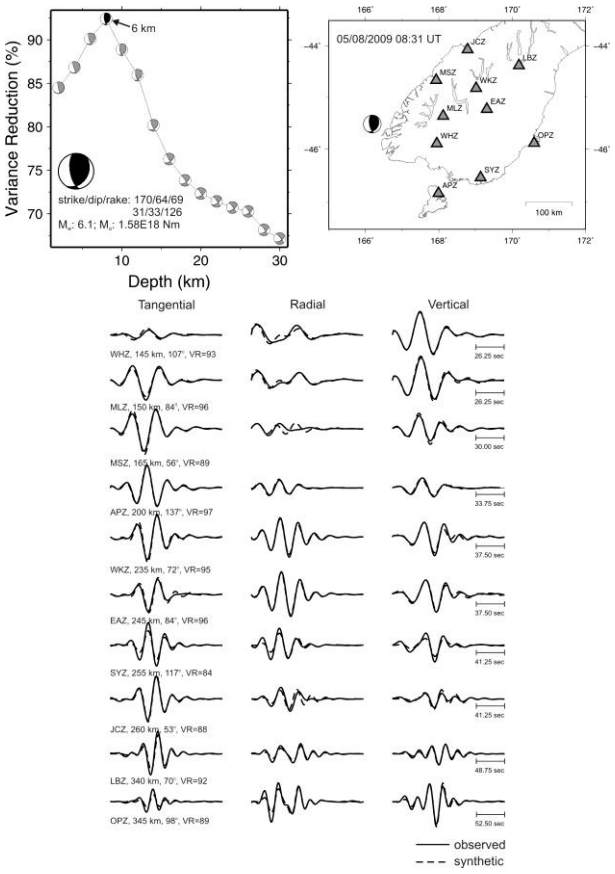

Figure 10: ***RMT solution for the largest aftershock (M_w 6.1) for which it was possible to calculate a RMT solution. Top left shows the variance reduction versus depth and the change in focal mechanism with depth. The best-fit is has a well defined maximum at 6 km and parameters for the best-fit solution are indicated in the figure. Top right shows the location of the event and the stations used to calculate the solution. Bottom shows the waveform fits for each station for the best-fit solution.***

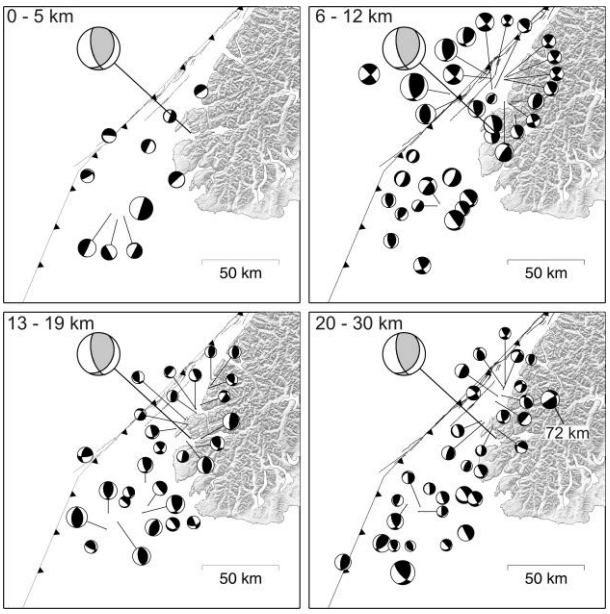

Figure 11: ***RMT solutions separated into depth ranges of 0-5 km, 6-12 km, 13-19 km and 20-30 km. The 20-30 km depth range also shows one solution with a depth of 72 km. The mainshock is shown in grey in each plot. The focal mechanisms show patterns which vary with depth as described in the text.***

Green's functions becomes more important. Because the inversion utilizes full waveforms from all three components, it can be done using only a few stations, although a greater number of stations with a good azimuthal distribution are preferred to reduce the effects of 3D structure.

More than 100 RMT solutions for aftershocks were calculated with the vast majority being within the first four days of the mainshock. Figure 10 shows waveform fits and changes in variance reduction and focal mechanism with depth for the largest aftershock for which a RMT solution could be calculated (M_w 6.1). The observed waveforms and Green's functions were typically bandpass filtered at 0.02 – 0.05 Hz, 0.02 – 0.06 Hz, 0.03 – 0.08 Hz or 0.05 – 0.10 Hz depending on the signal-to-noise ratio. For all events solutions are calculated over a range of depths to find the depth with the largest variance reduction between the observed and synthetic waveforms. Most of the aftershocks have a variance reduction of >~ 70% for the best-fit solution and many have a well defined maximum for the depth. This is very useful information as focal depths in the Fiordland region are often poorly constrained using standard location methods.

Figure 11 shows the RMT solutions plotted in four separate depth ranges. The focal mechanism used for the mainshock is taken from the Global CMT Project catalogue. The shallowest solutions (0-5 km depth) are all normal faulting mechanisms with one near-vertical fault plane and one near-horizontal. In the 6-12 km depth range the mechanisms are mainly reverse or strike-slip faulting with a P-axis oriented approximately E-W similar to the mainshock. Many of the strike-slip faulting mechanisms are located near the offshore extension of the Alpine Fault. Whether these events are on the Alpine Fault and induced by the Dusky Sound event or are unrelated to the Alpine Fault is an important question which will be examined in detail in future studies. The few normal faulting mechanisms in the 6-12 km depth range are quite shallow (~ 6 km) and are more related to the group at 0-5 km depth. At 13-19 km the mechanisms are mainly reverse faulting and very similar to the mainshock; therefore, they may also have occurred on the plate interface. At 20-30 km the mechanisms are a mixture of reverse, normal and strike-slip faulting

suggesting that the tectonic setting at greater depths becomes more complicated. Some events may be occurring in the crust above the plate interface and others within the subducting plate. Only one event is deeper than 30 km (as indicated in Figure 11) and is also the farthest east aftershock.

Geodetic Data

A wealth of geodetic data has been collected for measuring the permanent ground deformation associated with the earthquake. Using these data we can model the magnitude and distribution of slip on the fault surface that ruptured during the earthquake, and therefore better understand the implications of the earthquake for the tectonics of the Fiordland region and its effect on nearby faults.

All continuous GPS (cGPS) stations in the southern half of the South Island recorded displacements at the time of the earthquake, with the movement exceeding 300 mm at the nearest station (PYGR, Puysegur Point) and exceeding ~10 mm at eight stations as far away as Haast and Waimate (Figures 12 and 13). Only PYGR is in the near-field of the earthquake, so the cGPS data do not provide significant constraints on the slip distribution. They do, however, provide some constraint on the overall magnitude of the earthquake. A number of previously-occupied campaign GPS sites exist in the vicinity of the earthquake, and 27 of these were reoccupied over a 6-day period five weeks after the earthquake (Figure 12).

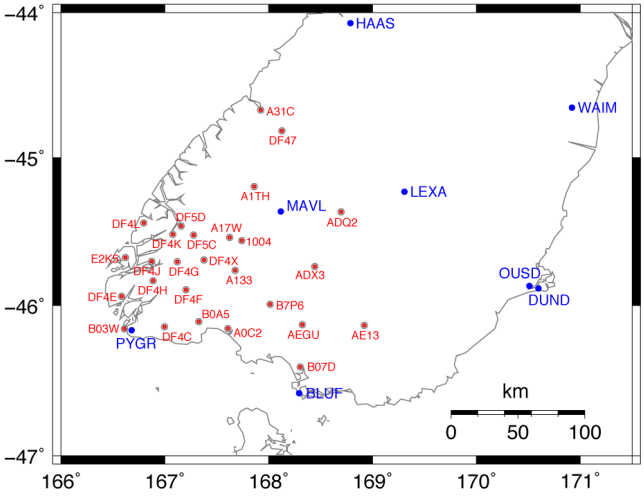

Figure 12: ***Continuous GPS sites (blue) that recorded more than 100 mm of permanent ground displacement as a result of the Dusky Sound earthquake. Campaign GPS sites (red) that were reoccupied 5 weeks after the earthquake.***

Satellite radar images have been taken over the earthquake region by the Synthetic Aperture Radar (SAR) instrument (PALSAR) on board the Japanese Space Agency's Advanced Land Observing Satellite (ALOS). We have so far processed three different post-earthquake scenes and combined them with pre-earthquake scenes to provide images of ground deformation during the earthquake, using the Differential Interferometric Synthetic Aperture Radar (DInSAR) technique

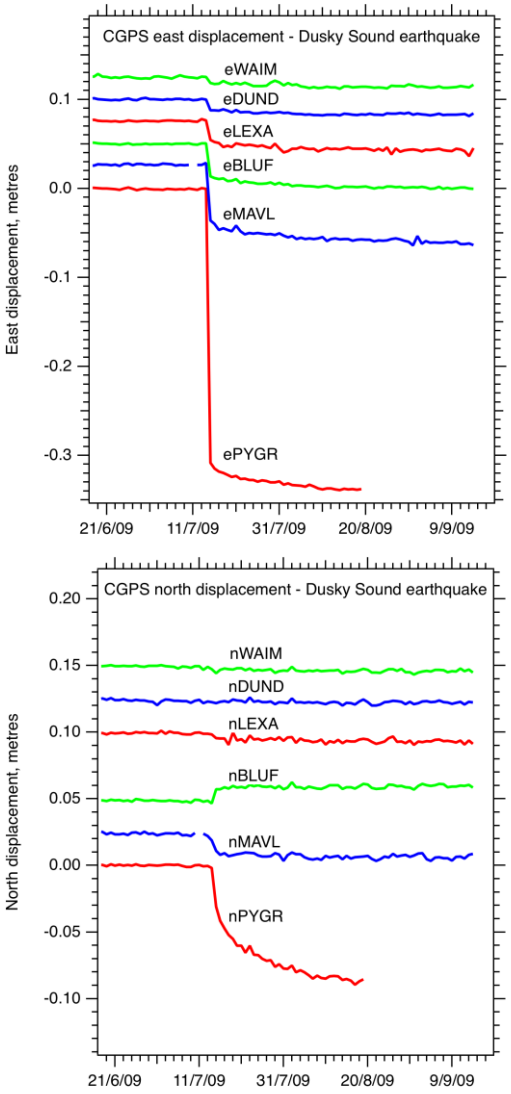

Figure 13: ***Time series of daily solutions for the east and north components of the six cGPS stations closest to the earthquake. The time series have been regionally filtered, and have had a linear trend removed so that the pre-earthquake data have zero slope. The westward and southward displacements (except at BLUF, which moves slightly north) are clearly visible, as is postseismic motion that continues for several weeks at some sites.***

(Massonnet *et al*, 1998, Rosen *et al*., 2000). As an example, one of these images is shown in Figure 14. The DInSAR system measures displacement along the line of sight from the ground to the satellite, so the measurement contains a mix of vertical displacement together with horizontal displacement along the azimuth from the ground to the satellite. The radar beam from PALSAR has an angle of incidence of 39º, so the instrument is about 20% more sensitive to vertical than to horizontal displacement.

DInSAR images (interferograms) are subject to a number of noise sources, in particular the following four. (1) Long-wavelength errors occur if the satellite orbit is not known

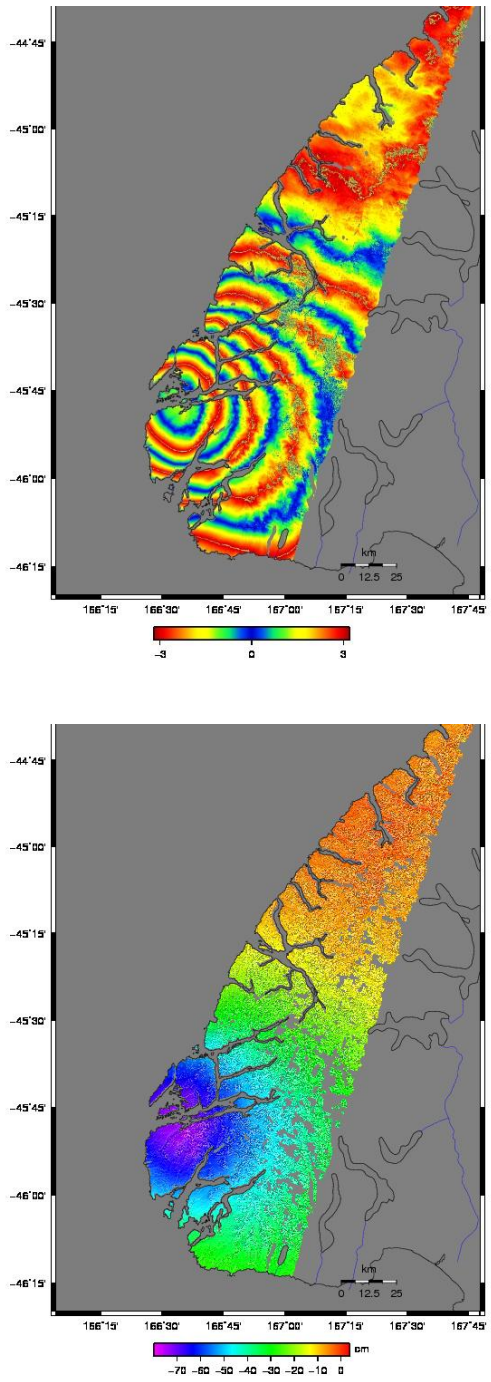

Figure 14: ***Satellite radar interferogram showing differences of satellite-ground distance before and after the earthquake. The upper image shows the original interferogram, where each coloured fringe represents 118 mm of apparent ground motion in the direction between the ground and the satellite. The lower image shows the same data after "unwrapping", indicate ~700 mm of motion away from the satellite in the vicinity of the epicentre. This implies a mix of ground subsidence and WNW horizontal motion.***

precisely. (2) The technique requires a correction for topography, and errors arise if the digital elevation model used in the processing is not exact. We have used the 40 m DEM provided by Land Information New Zealand (LINZ). The topographic errors are proportional to the "perpendicular baseline", or distance between the positions of the satellite when the before and after images are taken. For the images we have processed so far the baselines are between 400-1100 m, so any topographic error from this source should be small to moderate. (3) The radar signals are delayed as they pass through the ionosphere and through water vapour in the atmosphere, and these delays are indistinguishable from true ground displacement when only a pair of images is used to form an interferogram. (4) The nature of the ground surface causes changes in the phase of the reflected radar beam, and these are also indistinguishable from true ground displacement. This is of some concern for the Dusky Sound images, as they have been taken at different times of year, when snow depths in the more elevated regions of Fiordland are likely to be quite variable. However, given the amount of ground deformation caused by the earthquake, all of these noise sources are likely to be small compared to the size of the signal.

Geodetic Data Processing

The displacements at the cGPS sites are easily estimated as we have daily position solutions for these sites, and can take the difference between their positions on 14 July and 15 July. For the 15 July cGPS analysis we used only data following the earthquake, from 10:00-24:00 UT, for sites in the southern half of the South Island. It can be seen from Figure 13 that significant postseismic motion occurred at some sites, most notably on the north component of PYGR. We expect that this is due to continued afterslip on the fault rupture surface spreading southward from the main rupture area, but triggered slow slip on other nearby faults could also be an explanation. In measuring the coseismic offsets, we used regionally-filtered (Wdowinski *et al.*, 1997) versions of the cGPS time series in order to reduce common-mode signals and thus allow a more precise estimate of the offsets.

The displacements at campaign GPS sites are harder to estimate because of the several-year gap between the pre-earthquake and post-earthquake observations. In the case of the Fiordland region we are lucky to have several pre-earthquake observations at most sites that we can use to estimate the pre-earthquake motion of the site. However, many of these sites have been displaced by previous earthquakes, notably the 2003 M_W 7.2 Secretary Island earthquake, the 2004 M_W 8.1 Macquarie earthquake, and the 2007 M_W 6.7 Fiordland earthquake. We have made corrections to the pre-earthquake station positions based on (unpublished) dislocation models of these earthquakes. We then estimate the 2009 coseismic displacements by fitting a straight line to the pre-earthquake data, as shown by two examples in Figure 15. For each site we project the line and the uncertainty of the fit forward to the time of the post-earthquake GPS campaign, then subtract the measured position from the projected position to give the displacements shown in Figure 13. The maximum observed horizontal displacement is over 800 mm and the maximum vertical is more than 200 mm subsidence, both in the vicinity of Resolution Island.

We analysed the SAR data with Gamma software (Wegmüller and Werner, 1997) using standard DInSAR processing from raw format L1.0. The topographic signal was removed using the LINZ 40 m DEM. Orbits were not corrected. Information on the images is provided in Table 2. We show an example of one of the images in Figure 14. The image shows a lengthening of the apparent distance between the ground and the satellite that reaches more than 700 mm near Resolution Island. This represents a mixture of ground subsidence and horizontal ground displacement towards the west-northwest, and as such is qualitatively similar to the campaign GPS observations.

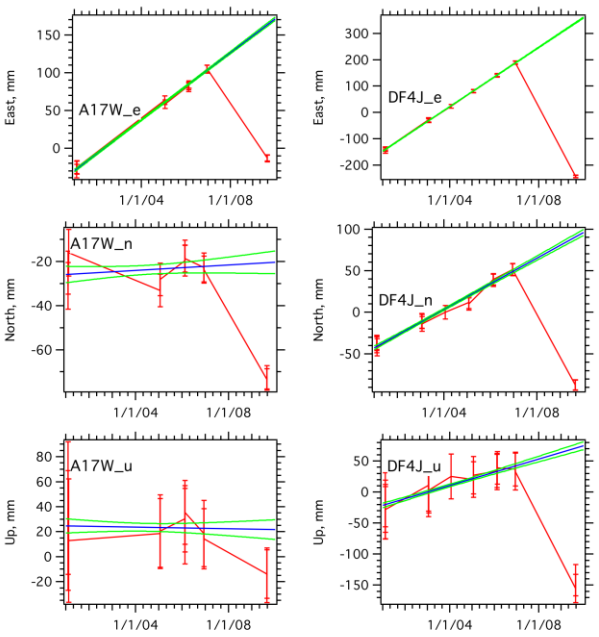

Figure 15: Two examples of the linear fit to pre-earthquake GPS site positions (east, north and up components), from which we estimate the displacement at the time of the earthquake taking into account the uncertainty in the forward-projected linear fit. Site A17W is near Te Anau and experienced about 200 mm displacement, while site DF4J is near Resolution Island and experienced more than 600 mm displacement.

Table 2. Collection information for SAR images.

Path	Frame	Direction	Date 1	Date 2	Baseline, m
349	6240-6250	Ascending	20090112	20090715	1129
639	4530-4550	Descending	20080720	20090723	420
348	6240-6250	Ascending	20090628	20090821	394

Modelling of Geodetic Data

We model the cGPS, campaign GPS and DInSAR data together to estimate the slip distribution and magnitude on the fault plane, which we assume from initial geodetic and seismic models to be the subduction interface between the obliquely descending Australian plate and the overlying Pacific plate. We use a profile of the subduction interface through the Dusky Sound epicentre as estimated from relocated microseismicity (Figure 16, M. E. Reyners, pers. comm., 2009) and extend this profile 120 km along strike to form the model fault surface. We divide the fault surface between 5 and 50 km depth into 5-km square cells and solve for the slip in each cell. We use linear inversion, closely following the methods adopted by Jonsson *et al.* (2002). We use Laplacian smoothing to stabilise the solution, choosing the weighting parameter for an optimum trade-off between misfit and solution roughness. We weight the slip magnitude towards zero at the lateral and lower boundaries of the fault surface, but put no constraints on the upper boundary. This is because we wish to test if the data can constrain the upper depth of significant slip.

Each interferogram contains millions of pixels, with nearby regions of the interferogram being highly correlated with each other and thus containing no independent information. We average the individual pixels into larger pixels of linear dimension ~100 m, then apply quadtree partitioning (e.g., Jonsson *et al.*, 2002) to further reduce the number of pixels while retaining the statistically significant part of the signal. The resulting data for inversion consist of: (1) 27 3D displacements from campaign GPS; (2) 14 3D displacements from cGPS (most of these are in the far-field so do not contribute much to the variable slip solution); (3) several hundred points in each of three InSAR images.

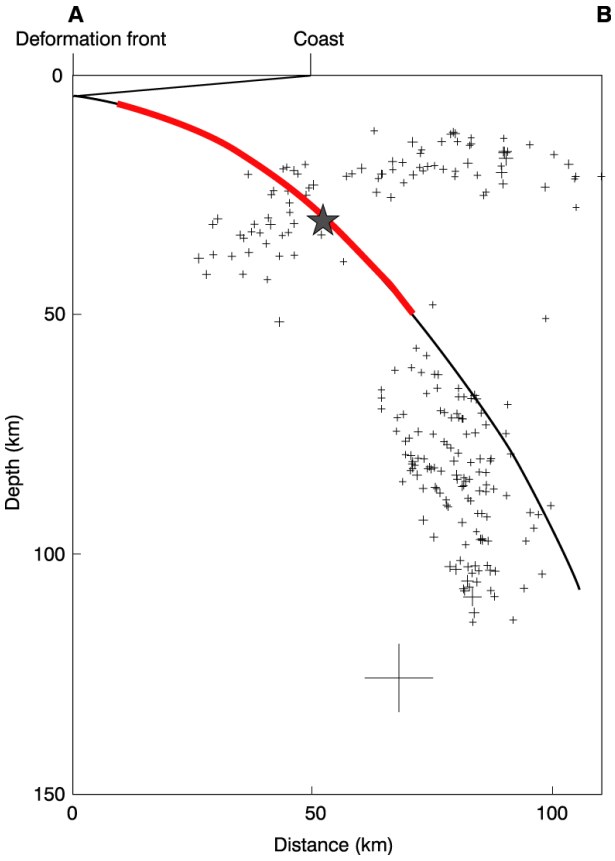

Figure 16: Subduction interface surface near the epicentre estimated from microseismicity relocated with a 3-D velocity model. We solve for slip between 6 and 50 km depth (red curve), and 120 km along strike assuming the interface geometry remains the same along that length.

In the modelling, we solve for an offset of each interferogram and also for a planar slope. The offset is essential as we do not know the zero point on the interferogram. The plane is intended to allow for any orbit errors, and also for the fact that the actual "look-angle" from the ground to the satellite varies by several degrees across the image. We have also

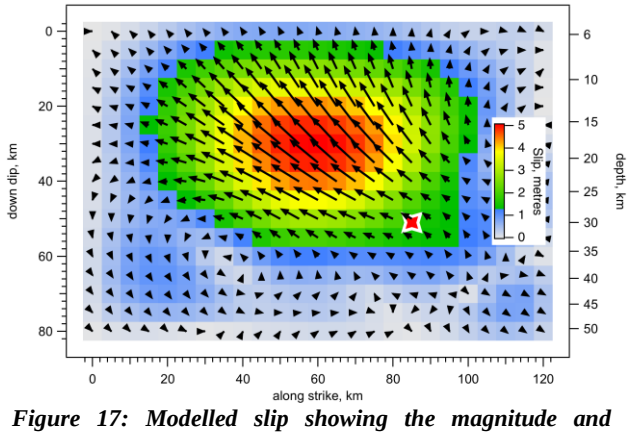

Figure 17: Modelled slip showing the magnitude and direction of slip on the fault surface. The image is looking down on the fault surface from the east-southeast; the southern end of the fault is to the left and the up-dip edge is

at the top. See Figure 19 for the map location of the fault surface. The red and white star is the GeoNet location of the hypocentre at 30.1 km depth. The left scale shows the distance down-dip from the centre of the uppermost fault patch, while the right scale shows the depth to the centre of each patch. The maximum slip is over 5 m. The slip direction rotates such that there is greater component of thrusting compared to strike-slip at shallower depths.

experimented with fitting a quadratic surface, but this makes only minor differences to the solution. We show a preliminary solution for slip on the fault surface in Figures 17, 18, and 19 along with the fit between the model predictions and the observations. A tsunami model using a slip distribution very similar to this one as the source provides an excellent fit to tsunami wave observations at an underwater pressure sensor (DART buoy) in the Tasman Sea (Prasetya *et al.*, 2010, submitted), giving confidence in the derived slip distribution. The observed and modeled subsidence in the vicinity of Resolution Island and Dusky Sound are both in the 200-250 mm range. Initial field surveys in the region for coastal uplift and subsidence detected inundation of salt marsh plants indicating the possibility of 100-150 mm subsidence, with 300 mm the maximum possible subsidence compatible with the observations. These observations are in good agreement with the geodetic data and models.

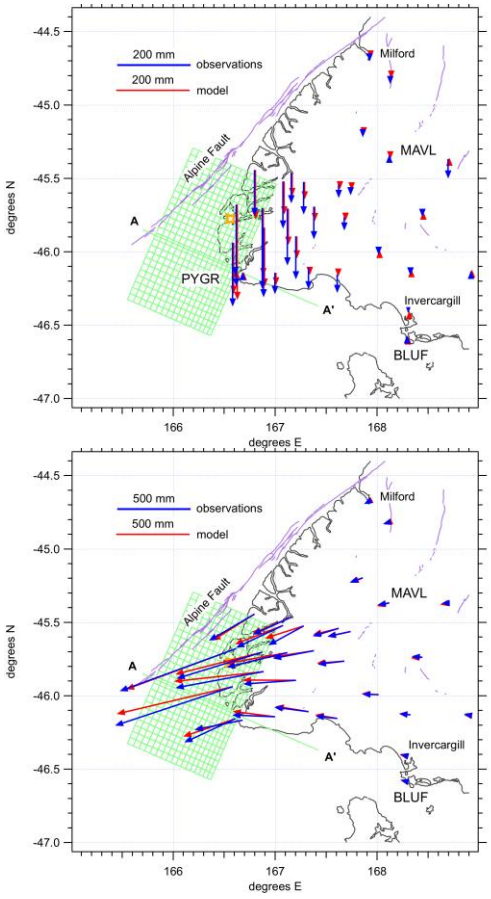

Figure 18: ***Comparison between observed and modelled horizontal (above) and vertical (below) displacements recorded at cGPS and campaign GPS stations. The blue arrows are the observations and the red ones are the model predictions. Some of the small disagreements between the observed and modelled campaign GPS displacements close to the earthquake may be due to postseismic afterslip that is present in the GPS data recorded 5 weeks after the earthquake, but not in the DInSAR data recorded within a week or so of the earthquake. The green mesh shows the projection to the ground surface of the patches in the fault slip model. The epicentre location is shown by the orange and white star.***

TSUNAMI

A tsunami resulting from the earthquake was observed and recorded in several ways: by the observations of the occupants of boats present in the sounds near the epicentre, by an Australian deep-ocean buoy in the Tasman Sea, and on tide gauges throughout the Pacific. In addition a post-event survey uncovered evidence of the environmental impact of the

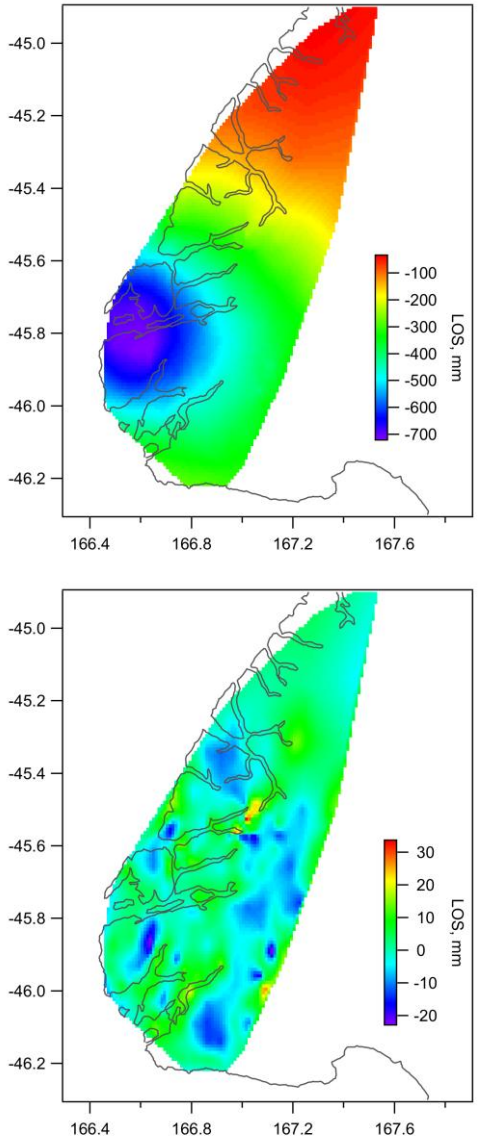

Figure 19: ***The upper image is the observed interferogram after reconstruction from the several hundred points in the quadtree decomposition (this is why the image looks slightly different to that in Figure 15). The lower image is the residual after subtracting the model fit. Note that the colour range is 700 mm on the left-hand image, but only 60 mm on the right-hand one.***

tsunami on specific locations within the sounds. A 1-metre tsunami was recorded at a tide gauge in Jackson's Bay, almost 300 km to the northeast of the epicentre. Subsequent field measurements based on surge deposits at Passage Point

document an approximately 2.3 metre wave. A deep-ocean buoy, operated by the Australian Bureau of Meteorology, in the Tasman Sea at 46.922 S 160.562 E recorded a long-period wave arriving 30 minutes after the earthquake. A good fit of the wave to that generated by the simulated tsunami from an M_w7.8 event provided early non-seismic confirmation of the seismically defined magnitude and location of the earthquake.

We have used the slip distribution model from our geodetic modelling as input for forward modelling of tsunami from the earthquake. Figure 20 shows the distribution of maximum wave amplitude during the 3 hours immediately following the mainshock.

The tsunami was recorded on several tide-gauges in New Zealand, Australia, and around the Pacific. At Jackson Bay the maximum amplitude was 500 mm (peak-to-trough 1m). Interestingly, the largest wave here was almost two hours after the initial arrival, a similar delay in the maximum wave was observed in 2003 following an M_w7.2 Fiordland earthquake located just to the north of the most recent event.

A field reconnaissance trip was undertaken from 19-21st August 2009, to assess the geological evidence of tsunami inundation and coastal deformation in Dusky Sound. In general there was surprisingly little evidence in the Dusky Sound area of the M_w 7.6 earthquake that had occurred just one month prior to the field visit. This is possibly due to a combination of the limited high-frequency shaking as previously discussed, and the robust nature of the Fiordland environment; rocky coastlines, hardy vegetation, very little infrastructure, solid bedrock and few areas of unconsolidated Quaternary sediments.

Seven locations around Dusky Sound were checked for evidence of coastal deformation and tsunami inundation. No evidence of coastal uplift was seen but possible evidence for 100 – 200 mm of coastal subsidence was seen. Evidence for this came from the inundation of coastal flora by 100 – 200 mm of water at extreme spring high tide levels but some of these species are salt-tolerant and may be inundated to such levels under typical spring high tide conditions. The best method of documenting the biological evidence of vertical coastal change is probably to revisit the sites in several months to compare the livelihood and elevation with respect to tide level of those species observed on this trip. For example, after several decimetres of coastal uplift in the Fiordland 2003 earthquake it took five months before the die-off of *Apophlaea lyalli* and other intertidal species was readily observable (U. Cochran, pers. comm., 2009). For example, at the head of Cascade Cove, on the southern side of Dusky Sound, much of the marginal vegetation was inundated at the peak of the spring high tide. The base of the *Juncus* spp. was submerged by approximately 100 mm, and some small toetoe (*Cortaderia* spp.) were also partially submerged. At several places beech tree roots were at the spring high tide level. Submergence of these plants may be normal for the extreme spring high tide conditions at the time but this is a location that would be worth visiting in several months time to check if there is any vegetation die-off.

Evidence for tsunami run-up was seen at Passage Point, and probable evidence was seen at Goose Cove. At Passage Point fish, shells, gravel and subtidal-dwelling-starfish were deposited 1.16 m above and 8 m inland of the spring high tide line. From the tidal charts for the Many Islands in Dusky Sound we estimate the tide was -0.15 m below mean sea level at the time of the earthquake. We assign this an uncertainty of ± 0.2 m to take into account the variation in tides between Many Islands and Passage Point. The elevation reached by the tsunami deposits suggests the tsunami at Passage Point was at least 2.3 ± 0.2 m in height. At Goose Cove, flattened pingao (golden sand sedge) up to 0.4 m above spring high tide on the barrier was probably bent over by currents associated with the withdrawal of the tsunami from the lagoon. Also seen near the flattened pingao were uprooted flax plants and a low grass bank with some plastered sand on it, these latter two features are more tenuously attributed to the tsunami. Many locations in Dusky Sound were checked for evidence of tsunami deposits, including Cormorant Cove and Luncheon Cove where eyewitnesses confirmed a tsunami occurred at these places. The nature of the Passage Point tsunami deposit suggests that the presence of loose, unconsolidated material on the beach face is an important requirement for leaving a tsunami deposit. Along the rocky coastlines that are prevalent in Dusky Sound there is little loose material to entrain. Therefore the lack of widespread tsunami deposits is not

Figure 20 (below): Modelled maximum tsunami amplitudes resulting from the Dusky Sound earthquake.

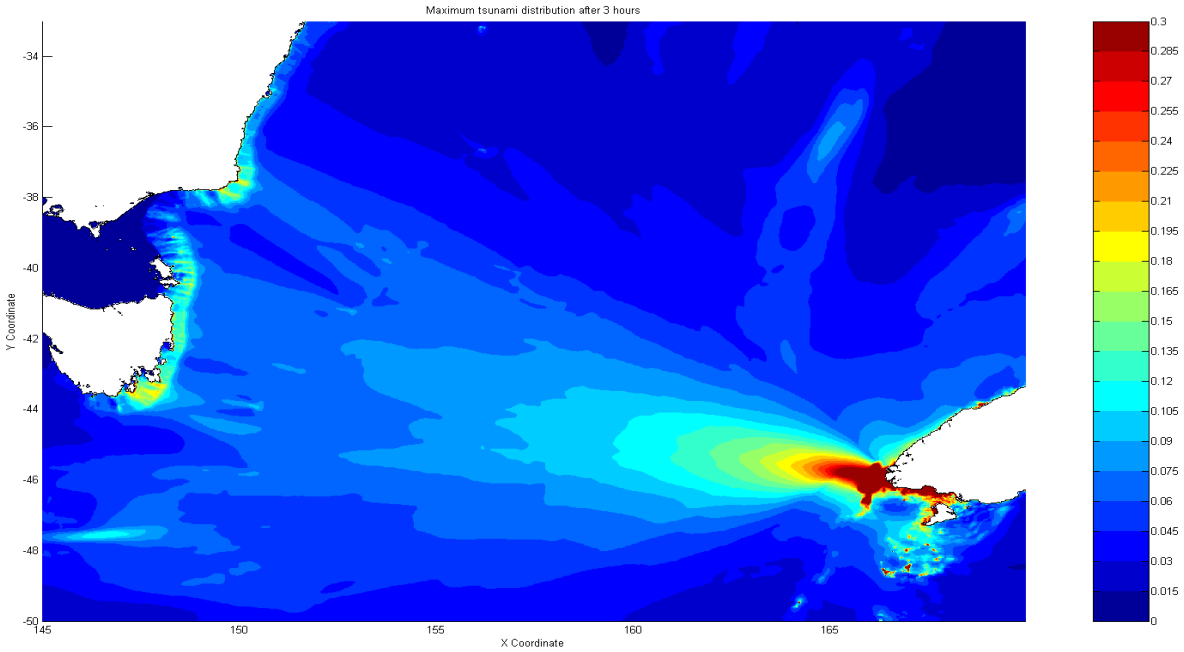

necessarily a reflection that the tsunami was not widespread, rather it is more likely that tsunami deposits were limited by the sediment sources available.

There are three confirmed or potential active fault traces within a 10 km radius of the earthquake epicentre. Although the main earthquake rupture was at depth on the plate interface, it was considered possible that it triggered secondary slip on the nearby upper plate faults. Accordingly we checked each of the three fault traces for any evidence of fresh surface offset but no recent surface rupture was seen.

LANDSLIDES

At least 241 landslides were mapped during the helicopter reconnaissance flights over the area affected by the earthquake with accuracy varying from plus or minus ~500 m for distant landslides to a few metres for those closer to the flight path. Landslides triggered by the earthquake ranged from small superficial failures involving a few trees and a few tens of cubic metres of soil, to larger shallow landslides with estimated volumes of 10^3–10^5 m^3 of bedrock and regolith and extending ~1000 m downslope. The landslides were ranked according to size on a scale of 1 to 3 (Figure 21), following the approach by Hancox *et al.* (2003) for the August 2003 earthquake. On this scale 1 is small; 2 is for larger (moderate) failures with greater area, length and volume; and 3 is the largest, usually involving bedrock, with lengths of > 500 m and widths > 100 m.

The total area affected by landslides triggered by the July 2009 earthquake is at least ~5600 km^2, and extends from the epicentre in Dusky Sound to ~70 km north to Doubtful Sound, 40 km south to Preservation Inlet, and 75 km east to Lake Hauroko (Figure 21). The main area of landsliding covers an area of about 2000 km^2. As expected, the density of landsliding decreases with distance away from the epicentre.
The largest landslides occurred in areas of steep terrain southeast of Dusky Sound, about 20 km from the epicentre. One of the larger landslides in that group is a reactivation of the very large, prehistoric (possibly 1826) landslide that dams Lake Purser (Figure 22). Moderate-size landslides are common in the area of between Breaksea Sound and the inner Dusky Sound, ~25 km east-northeast of the epicentre. A number of landslides on the steep coastal cliffs of Five Fingers Peninsula southwest of Resolution Island appear (from 2004 satellite images) to be mainly small and moderate-sized reactivations of slope failures that pre-date the 2003 earthquake.

The absence of larger landslides in this area and the immediate vicinity of the epicentre probably reflects the relatively low topographic relief in the outer Dusky Sound and Resolution Island area. A cluster of small to moderate-size landslides which occurred ~50 km northeast, in the Crooked Arm and First Arm area of Doubtful Sound and other landslides in this area, appear to be related to steeper terrain and previous slope failures in the area. Many of the larger landslides east of Dusky Sound appear to be reactivations of 2003 and older landslide scars (Figures 23 and 24). The head of one such landslide at the head of First Arm was reactivated, but other nearby 2003 landslides were not obviously affected (Figure 25). Typically, less than ~20% of the 2003 landslides appear to have been reactivated.

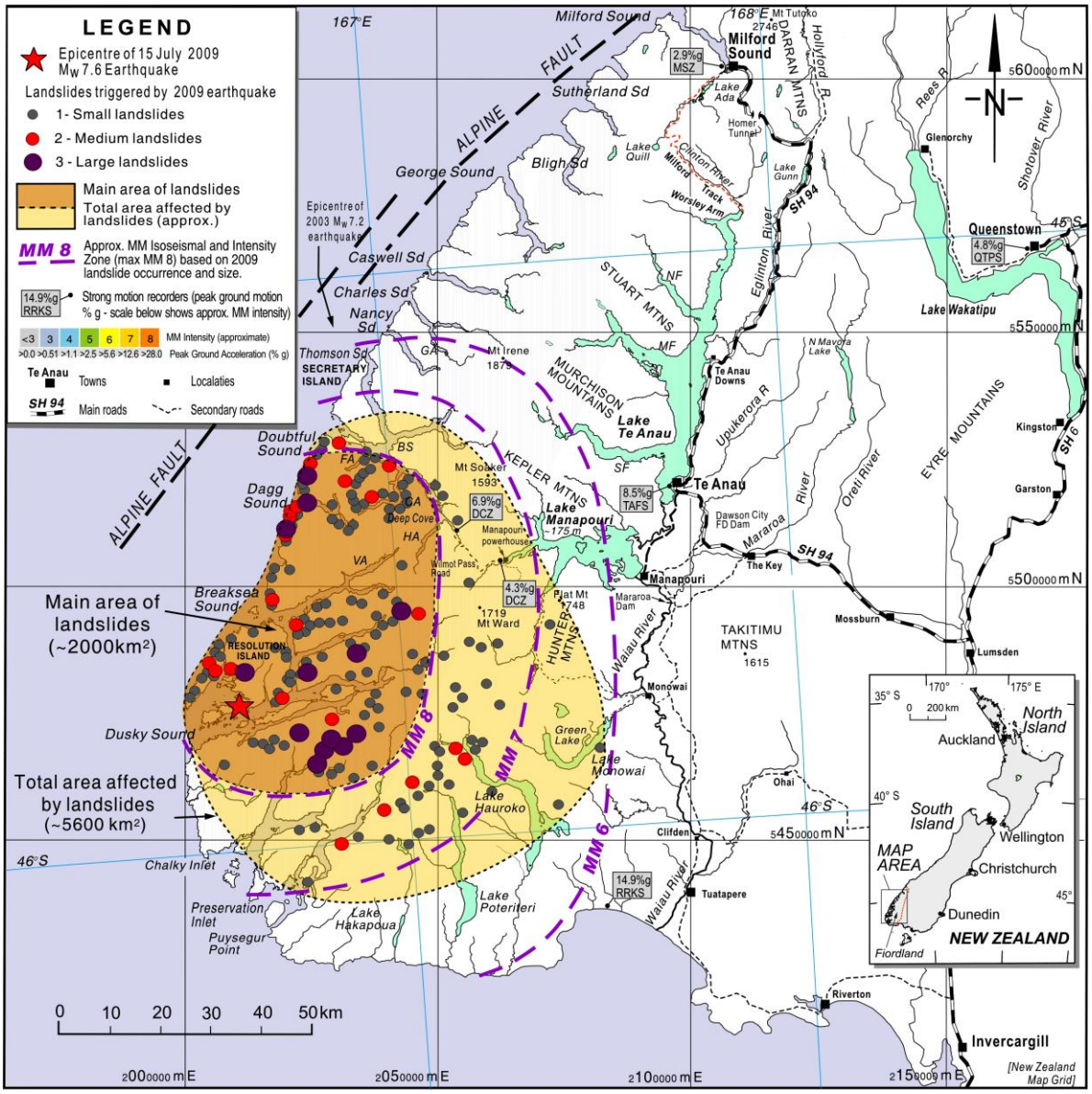

Figure 21: ***Map showing the locations and distribution of landslides triggered by the M_w 7.6 Dusky Sound earthquake of 15 July 2009 (epicentre shown by the red star). Approximate Modified Mercalli (MM) felt intensity isoseismals have been assigned from environmental criteria.***

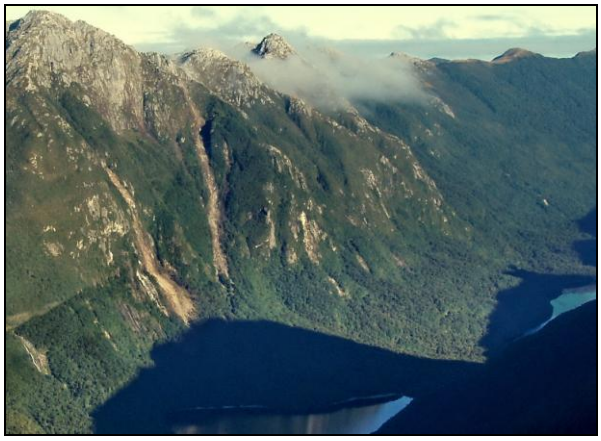

Figure 22: The head of the very large (~30 Mm^3) prehistoric landslide (left) which dams Lake Purser (bottom), 20 km southeast of the epicentre, was partly reactivated by the 2009 earthquake, but not by the 2003 earthquake. This minor reactivation was one of the larger slope failures triggered by the 2009 earthquake.

Figure 23: This large rockfall (centre) near the head of Wet Jacket Arm ~35 km from the epicentre was also triggered by the 2009 earthquake. Smaller failures at the top of the slope (left) probably also occurred in 2009 as they are not present on 2007 satellite images.

Figure 24: ***The head of this large 2003 landslide (centre) at the head of First Arm was reactivated by the 2009 earthquake, but the 2003 landslide to the left and others nearby were not obviously affected. Less than ~20% of the 2003 slides appear to have been significantly reactivated by the 2009 earthquake. This is currently being investigated using satellite imagery.***

DISCUSSION

The M_w 7.6 Dusky Sound earthquake generated relatively little damage compared to worldwide events of this magnitude. Seismic recordings show relatively little high-frequency content. The earthquake also triggered few landslides, about half of the amount triggered by the 2003 M_w 7.2 Fiordland earthquake. Analysis of the focal mechanism suggests that the southwestward directivity of the rupture focussed much of the radiated energy offshore. The event generated a locally dangerous tsunami. Stress calculations predict that the mainshock loaded the southernmost Alpine Fault by about 2 bars. More work is necessary to better understand the increased risk of an Alpine Fault rupture based on this stress loading.

ACKNOWLEDGEMENTS

We thank GeoNet, EQC and LINZ for the operation and financial support of the cGPS network, LINZ for participation in and partial support of the post-earthquake GPS campaign, and Otago University Survey School for their major contributions to the pre-earthquake GPS campaigns.

The ALOS PALSAR data has been used in this work with the permission of JAXA and METI and the Commonwealth of Australia (Geoscience Australia) ("the Commonwealth"). JAXA, METI and the Commonwealth have not evaluated the data as altered and incorporated within this work, and therefore give no warranty regarding its accuracy, completeness, currency or suitability for any particular purpose.

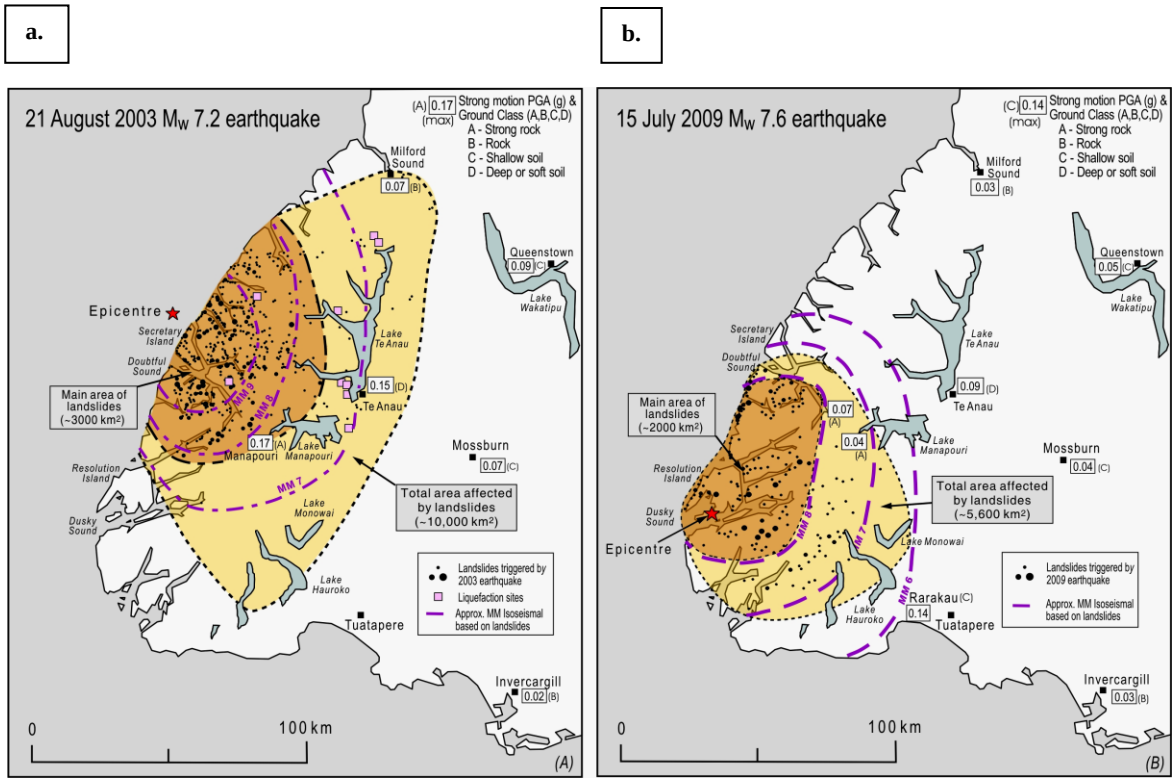

Figure 25: ***Maps showing landslide distributions, MM intensities, and strong motions recorded for the August 2003 (a) and July 2009 (b) Fiordland earthquakes. The density and extent of landslides was much greater for the smaller (M_w 7.2) 2003 earthquake, than it was for the M_w 7.6 earthquake in 2009. Soil liquefaction occurred during the 2003 earthquake, but not the 2009 event.***

REFERENCES

Bowman, D. D. & King, G. C. P., (1995). "Accelerating seismicity and stress accumulation before large earthquakes," *Geophysical Research Letters*, **28**, 4039-4032.

Bowman, D. D., Ouillon, G., Sammis, C. G., Sornette, A. & Sornette, D., (1998) "An observational test of the critical earthquake concept". *Journal of Geophysical Research*, **103**, 24359-24372.

Choy, G.L., McGarr, A., Kirby, S.H. and Boatwright, J., (2006). "An overview of the global variability in radiated energy and apparent stress". *Geophysical Monograph*, **170**: 43-57.

Christensen, D.H. and Ruff, L.J., (1983). "Outer-rise earthquakes and seismic coupling." *Geophysical Research Letters*, **10**(8): 697-700.

DeMets, C., Gordon, R.G., Argus, D.F. and Stein, S., (1994). "Effect of recent revisions to the geomagnetic reversal time scale on estimates of current plate motions". *Geophysical Research Letters*, **21**(20): 2191-2194.

Doser, D.I., Webb, T.H. and Maunder, D.E., (1999). "Source parameters of large historical (1918-1962) earthquakes, South Island, New Zealand." *Geophysical Journal International*, **139**(3): 769-794.

Dowrick, D.J., Hancox, G.T., Perrin, N.D., Dellow, G.D., (2008). "The Modified Mercalli Intensity Scale – Revisions arising from New Zealand experience". *Bulletin of the New Zealand Society for Earthquake Engineering*, Vol. **41**, No. 3, September 2008, pp 193–205.

Dreger, D. & Helmerberger, D. V., (1993). "Determination of source parameters at regional distances with single station or sparse network data". *Journal of Geophysical Research*, **98**, 8107-8125.

Dreger, D. S., (2003). "TDMT_INV: Time Domain Seismic Moment Tensor INVersion" *International Handbook of Earthquake and Engineering Seismology*, 81B, 1627.

Eberhart-Phillips, D. and Reyners, M., (2001). "A complex, young subduction zone imaged by three-dimensional seismic velocity, Fiordland, New Zealand." *Geophysical Journal International*, **146**(3): 731-746.

Guerrieri, L., Vittori, E., (2007). "Intensity Scale ESI (Environmental Seismic Intensity Scale)" 2007. Memorie Descriptive Della Carta Geologica d'Italia, 74, Servizio Geologico d'Italia – Dipartimento Difesa del Suolo, APAT, Rome, Italy.

Hancox, G.T., Cox, S.C., Turnbull, I.M., Crozier, M.J., (2003). "Reconnaissance studies of landslides and other ground damage caused by the Mw7.2 Fiordland earthquake of 22 August 2003". *Institute of Geological & Nuclear Sciences science report* 2003/30, 32 p.

Hancox, G.T., Perrin, N.D., (2009). "Green Lake Landslide and other giant and very large postglacial landslides in Fiordland, New Zealand". *Quaternary Science Reviews: Special Issue "Natural hazards, extreme events, and mountain Topography*", Volume **28**, Issues 11–12, June 2009, pp 1020–1036.

Jaume, S. C. & Sykes, L. R., (1999). "Evolving toward a critical point : A review of accelerating seismic moment/energy release prior to large and great earthquakes". *Pure and Applied Geophysics*, **155**, 279-305.

Jonsson, S., Zebker, H., Segall, P. & Amelung, F., (2002). "Fault slip distribution of the Hector Mine earthquake estimated from satellite radar and GPS measurements", *Bulletin of the Seismological Society of America*, **92**, 1377-1389.

King, G. C. P. & Cocco, M., (2001). "Fault interaction by elastic stress changes: New clues from earthquake sequences" *Advances in Geophysics*, **44**, 1-38.

Massonnet, D. & Feigl, K., (1998). "Radar interferometry and its application to changes in the Earth surface", *Reviews of Geophysics*, **36**, 441-500.

McVerry, G. H., Zhao, J. X., Abrahamson, N. A. & Sommerville, P. G., (2006). "New Zealand acceleration response spectrum attenuation relations for crustal subduction zone earthquakes" *Bulletin of the New Zealand Society for Earthquake Engineering*, **39** (1): 1-58.

Pasyanos, M. E., Dreger, D. S. & Romanowicz, B., (1996). "Towards real-time determaination of regional moment tensors", *Bulletin of the Seismological Society of America*, **86**, 1255-1269.

Prasetya, G., Beavan, J., Wang, X., Reyners, M., Power, M., Wilson, K. and Lokovich, B., "Evaluation of the July 15, 2009 Fiordland, New Zealand tsunami in the source region", submitted to *Pure & Applied Geophysics*.

Reyners, M., McGinty, P., Cox, S., Turnbull, I., O'Neill, T., Gledhill, K., Hancox, G., Beavan, J., Matheson, D., McVerry, G., Cousins, J., Zhao, J., Cowan, H., Caldwell, G., Bennie, S. and the GeoNet team, (2003). "The MW 7.2 Fiordland earthquake of August 21, 2003: background and preliminary results". *Bulletin of the New Zealand Society for Earthquake Engineering*, **36**(4).

Ristau, J., (2008). "Implementation of routine regional moment tensor analysis in New Zealand". *Seismological Research Letters*, **79**, 400-415.

Robinson, R., Zhou, S., Johnston, S. & Vere-Jones, D., (2005). "Precursory accelerating seismic moment release (AMR) in a synthetic seismicity catalog: A preliminary study". *Geophysical Research Letters*, **32**, L07309.

Rosen, P., Hensley, P., Joughin, I., Li, F., Madsen, S., Rodriguez, E. & Goldstein, R., (2000). "Synthetic aperture radar interferometry", *Proceedings of the IEEE*, **88**, 333-382.

Stein, R. S., (1999). "The role of stress transfer in earthquake occurrence". *Nature*, **402,** 6762, 605-609.

Van Dissen, R., Cousins, J., Robinson, R., Reyners, M., (1994). "The Fiordland earthquake of 10 August 1993". *Bulletin of the New Zealand Society for Earthquake Engineering* **27**: 147-154.

Wdowinski, S., Bock, Y., Zhang, J., Fang, P. and Genrich, J., (1997). "Southern California Permanent GPS Geodetic Array: Spatial filtering of daily positions for estimating coseismic and postseismic displacements induced by the 1992 Landers earthquake", *Journal of Geophysical Research*, **102**, 18,057-18,070.

Wegmüller, U. & Werner, C., (1997). "Gamma SAR processor and interferometry software", *Third ERS Symposium on Space at the service of our Environment, Florence, Italy.*